Improvement of Thermoelectric Properties via Texturation Using a Magnetic Slip Casting Process-The Illustrative Case of CrSi2

Sylvain Le Tonquesse, Wenhao Zhang, Bhuvanesh Srinivasan, Bruno Fontaine, Takanobu Hiroto, Takao Mori, Jean-François Halet, David Berthebaud, Tohru S. Suzuki

Improvement of Thermoelectric Properties via Texturation using a Magnetic Slip Casting Process – the Illustrative Case of $CrSi_2$

Sylvain Le Tonquesse,[*,†] Wenhao Zhang,[‡,¶] Bhuvanesh Srinivasan,[†] Bruno Fontaine,[§] Takanobu Hiroto,[‖] Takao Mori,[‡,¶] Jean-François Halet,[†] David Berthebaud,[*,†] and Tohru S. Suzuki[*,‖]

†*CNRS-Saint-Gobain-NIMS, IRL 3629, Laboratory for Innovative Key Materials and Structures (LINK), National Institute for Materials Science, Tsukuba 305-0044, Japan*

‡*National Institute for Materials Science (NIMS), WPI-MANA, 1-1-1 Namiki, Tsukuba 305-0044, Japan*

¶*Graduate School of Pure and Applied Science, University of Tsukuba, Tsukuba, Ibaraki 305-8671 Japan*

§*Univ Rennes, CNRS, Ecole Nationale Supérieure de Chimie de Rennes, ISCR-UMR6226, F-35000, Rennes, France*

‖*National Institute for Materials Science (NIMS), 1-2-1 Sengen, Tsukuba, Ibaraki, 305-0047, Japan*

E-mail: Sylvain.LETONQUESSE@cnrs.fr; David.BERTHEBAUD@cnrs.fr; SUZUKI.Tohru@nims.go.jp

Abstract

Transition metal silicides constitute a promising class of inexpensive and non-toxic thermoelectric materials showing competitive properties. This article reports an ef-

ficient process to synthesize highly textured poly-crystalline $CrSi_2$ by performing slip casting under a strong magnetic field. The crystallographic texture of spark plasma sintered samples, characterized by electron back-scattered and X-ray diffraction techniques showed a fiber texture symmetry with the *c*-axis of hexagonal $CrSi_2$ aligning preferentially along the magnetic field direction. The thermoelectric properties measured both parallel and perpendicular to the *c*-axis texture direction showed a large anisotropy. In particular, a significantly higher Seebeck coefficient was measured $\|c$ reaching a maximum value of 200 μV K^{-1} at 650 K, inducing a power factor $\|c$ twice higher than $\perp c$ with an average value of 2.2 mW m^{-1} K^{-2}. Density functional theory and transport property calculations revealed that an anisotropic two-band model can explain the higher thermoelectric property along the *c*-axis direction, which can be traced to Cr-Cr bonding interactions along this direction. The estimated thermoelectric figure of merit $ZT_{\|c}$ was improved to 0.20 at 773 K. This is 50 % higher than that measured for randomly oriented samples and comparable to that observed for single crystals. Such a performance boost can certainly be reiterated for other types of thermoelectric materials using the efficient magnetic slip-casting process reported in this article.

1 Introduction

Thermoelectric (TE) materials, which enable the conversion of waste heat into electricity, have been the object of extensive investigations over the past, with the aim to increase the efficiency of current fossil fuel combustion technology. The conversion efficiency of TE materials is directly linked to their figure of merit *ZT* given by:

$$ZT = \frac{\alpha^2 T}{\rho \kappa} \tag{1}$$

with α the Seebeck coefficient, ρ the electrical resistivity, κ the thermal conductivity and T the absolute temperature. In the last decade, mid-temperatures (600 - 800 K) thermoelectrics such as PbTe[1], GeTe[2,3], SnTe[4], $CoSb_3$-based skutterudites[5,6] and SnSe[7,8] with

high $ZT > 1.5$ have been reported. Despite this recent breakthrough, the use of these materials for large-scale industrialization remains impracticable as they are composed of rare, expensive or toxic constituting elements[9]. Moreover, the requirement for good mechanical properties, chemical and thermal stability and low density reduces even more the number of possible candidates. Transition metal silicides (TMS) such as $CrSi_2$, the low-temperature phase β-$FeSi_2$ and $MnSi_{1.74}$, extensively studied nowadays both in the academics[10–12] and the industry[13–15] constitute viable alternatives. TMS are characterized by high power factors $PF = \alpha^2/\rho$ but their maximum ZT remain moderate (0.13 for $CrSi_2$[16], 0.20 for doped β-$FeSi_2$[17] and 0.45 for $MnSi_{1.74}$[18]) due to high thermal conductivities[19]. For these reasons, the majority of published works related to TMS focused on reducing κ using common strategies such as alloying[20–22], nanostructuration[23,24], thin films[25], and composite synthesis[26–30]. Employing these strategies, enhanced maximum $ZT \approx 1$ (+ 150 %) for Re-doped $MnSi_{1.74}$[31,32] or $ZT = 0.25$ (+ 70 %) for Ge-doped $CrSi_2$[20] were achieved for instance. However, these promising results were often obtained at the expense of increased cost or reduced thermal stability.

An alternative approach to enhance ZT consists in the texturation of bulk polycrystalline TMS along preferential crystallographic directions. Most thermoelectric TMS are known to exhibit intrinsically large anisotropy of their TE properties[33]. For example, $MnSi_{1.74}$ (tetragonal) and $CrSi_2$ (hexagonal) single crystals show PF that are about 40 % higher along the a- and c-axes, respectively, mostly due to higher Seebeck coefficients[34,35]. Inducing large texturation in polycrystalline materials should result in macroscopic properties comparable to single crystals without the inherent high processing cost of the latter which strongly reduces potential industrial applications. Texturation processes reported for TMS mostly consist in sintering pellet or ribbon shaped particles under uniaxial pressure, the particle morphology being produced by cleaving large crystals along preferential crystallographic planes[34,36] or by melt-spinning process[37]. However, the properties remain close to randomly oriented materials due to the relatively small texturation strength. The crystal-

lization of an Mn-Si melt under a magnetic field of 3 T was also used to produce textured $MnSi_{1.74}$ polycrystalline ingots[38]. According to the authors, the electrical resistivity $\perp c$ was twice lower than for randomly oriented samples synthesized without magnetic field. However, the resulting *PF* of 0.2 mW m^{-1} K^{-2} is about five times lower than reference samples from the literature due to a large amount of a secondary phase. Other thermomechanical processes such as rolling or hot-extrusion, which have been successfully used for other TE materials such as Bi_2Te_3[39], oxides[40] and oxi-chalcogenides[41], are not applicable to TMS due to their purely elastic mechanical behaviors. These literature results show that inducing high texturation of TMS samples is a promising method to increase their TE performances but also that appropriate texture processes remain to be developed.

Here, an efficient texturation process is proposed which consists in slip casting a dispersion of $CrSi_2$ particles under a strong magnetic field (12 T). This process takes advantage of the diamagnetic anisotropy of the materials to align the freely moving particles in suspension along their easy magnetization axis[42]. In addition, slip casting processes make possible the fabrication of large scale near net-shape parts which is of uttermost importance for efficient industrialization. The oriented green body obtained after slip casting can be further processed to obtain a fully dense textured sample. Such a process has already been successfully applied to oxides[43,44], carbides[45–47], nitrides[48,49] and borides[50] for instance but rarely to TMS[51,52]. Indeed, $CrSi_2$ is a good candidate to demonstrate the usefulness of this texturation method for TE TMS because to our knowledge, (i) no data is available in the literature on textured polycrystalline samples, (ii) its congruent melting facilitates the synthesis of large amount of material prepared by conventional fusion/solidification processes, and (iii) it has a simple crystal structure compared to others TMS ($MnSi_{1.74}$ has an aperiodic crystal structure[53,54] and β-$FeSi_2$ presents stacking faults[55]) which make easier the realization of texture analyses. In this article, the texturation process is first described in detail and the optimal synthesis conditions are discussed. The texture of the

samples were quantitatively analyzed using both electron backscattered diffraction (EBSD) and X-ray diffraction (XRD) techniques. The directional TE properties were measured and compared to a randomly oriented reference as well as single crystal data from the literature. The computed band structure and the transport properties of $CrSi_2$ are discussed in order to better understand the origin of the strong anisotropy in this material.

2 Experimental procedure

2.1 Synthesis

$CrSi_2$ was synthesized by arc-melting Cr chips (Aldrich Chemicals, 99.995 %) and Si pieces (Aldrich Chemicals, 99.95 %) in stoichiometric amount using a home-made furnace apparatus. The furnace chamber was purged three time with Ar and the resulting ingot of about 1.5 cm^{-3} was flipped and remelted four times to ensure good homogenization. The weight loss was under 0.2 wt.%. The $CrSi_2$ ingot was then pulverized into powder by wet ball-milling using a Fritsch Pulverisette 7 and Y-stabilized ZrO_2 jar and balls (Ø= 5 mm). The ball-to-powder weight ratio was set to 5, the jar was filled with ethanol at 15 vol.% and the milling was performed at 200 rpm for 8 h. The ball-milled powder was dried overnight at 373 K. A slurry containing 20 wt.% solid load was prepared by dispersion of the $CrSi_2$ powder in absolute ethanol. 0.3 wt.% of polyethylenimine (PEI) dispersing agent (Sigma Aldrich, average M = 10000 g mol^{-1}, linear chains) was added to the slurry and the acidity was adjusted with 0.1 vol.% of acetic acid to reach an equivalent pH of 5.5. The breaking of the aggregates was ensured by thoroughly sonicating the slurry. The later was poured in the slip casting set-up consisting of a cylindrical polyethylene mold (Ø= 12 mm, height = 40 mm) placed on a porous alumina plate (25 % porosity) covered with a membrane filter (200 nm pores size). The mold containing the slurry was covered with a plastic film in order to prevent evaporation of ethanol. The slip casting set-up was placed inside a 12 T superconducting magnet either in vertical or horizontal position. The green bodies were first densified by cold isostatic pressing (CIP) at 394 MPa for 10 min then by

spark plasma sintering (SPS) in a Ø = 10 mm graphite die at 1523 K (heating and cooling rate of 50 K min^{-1}) and 80 MPa for 10 min.

2.2 Powder and slurry characterizations

The grain size distribution of the ball-milled powder was determined by the dynamic light scattering (DLS) technique using a Microtrac Nanotrac ULTRA apparatus. Zeta-potentials were measured using a Malvern Nano Essentials zetasizer. The viscosity was measured using a Tokisangyo RE-215L viscometer.

2.3 X-ray diffraction analyses

XRD analyses were performed using a Rigaku TTRIII diffractometer equipped with a rotating Cu anode ($\lambda_{K\alpha1}$ = 1.5406 Å and $\lambda_{K\alpha2}$ = 1.5444 Å with a ratio $I_{K\alpha2}/I_{K\alpha1}$ of 0.5, 45 kV and 150 mA) and a D/teX Ultra detector. XRD texture analyses were performed using a Rigaku SmartLab diffractometer equipped with χ-ϕ attachment, a rotating Cu X-ray anode ($\lambda_{K\alpha1}$ = 1.5406 Å and $\lambda_{K\alpha2}$ = 1.5444 Å with a ratio $I_{K\alpha2}/I_{K\alpha1}$ of 0.5, 45 kV and 200 mA) and a HyPix-3000 detector. For XRD texture measurements, $2\theta/\theta$ scans were measured in the range 5° - 130° with a step size of 0.02°. The χ angle was measured in the range 0° - 45° with a step size of 5° for all samples and the ϕ angle was measured in the range 0° - 180° with a step size of 5° for $CrSi_2$-h and kept constant for $CrSi_2$-r and $CrSi_2$-v. Refinement of the XRD patterns and texture analyses were performed using the *MAUD* software[56].

2.4 Scanning electron microscopy analyses

Back-scattered electron images and elemental energy dispersive spectroscopy (EDS) analyses of the sintered pellets were performed with a scanning electron microscope (SEM) Hitachi Tabletop TM3000. Particle morphology and EDBS mapping were realized using a JEOL JSM7000F SEM microscope equipped with a field-emission electron source. Samples preparation for EBSD consisted in successive polishings with silicon carbide, diamond and colloidal silica.

2.5 Thermoelectric properties measurements

Thermal diffusivity (D) measurement was performed under N_2 atmosphere on Ø = 10 mm and 1 mm thick samples coated with graphite using a laser flash analysis (LFA) apparatus Netzsch 467 HyperFlash. The thermal conductivity was calculated using the expression $\kappa = D{\cdot}C_p{\cdot}d$ with D the thermal diffusivity, d the density and C_p the specific heat. C_p was calculated using the Dulong-Petit law $C_p = 3{\cdot}N{\cdot}R/M = 0.69$ J g^{-1} K^{-1} with N=3 the number of formula per unit cell, R the ideal gas constant and M the molar mass. d was determined by the Archimede method in absolute ethanol. The Seebeck coefficient and electrical resistivity were measured simultaneously on $9\times1\times2$ mm^3 bars using a ZEM5 equipment under partial He atmosphere. The Hall coefficient (R_H) was measured in AC mode using a physical property measurement system (PPMS, Quantum Design) with a magnetic field sweeping from -5 T to +5 T. The charge carrier concentration n of the sample $CrSi_2$-r was calculated from the expression $n = 1/eR_H$ with e the elementary charge of the electron.

2.6 Computational details

2.6.1 DFT band structure calculations

Density Functional Theory (DFT) calculations were carried out on diamagnetic $CrSi_2$ using the *Quantum Espresso* package[57,58]. The cell parameters and atomic positions were fixed at their experimental values ($CrSi_2$-r in Table 1). The generalized gradient approximation Burke, Perdew and Ernzerhof (PBE) functional[59] and the projector augmented-wave (PAW) method[60] were used. A kinetic energy cutoff of 200 Ry and a ten-times higher charge density cutoff were used for the calculations as a result of the convergence tests. Convergence threshold energy for self consistent calculations was 1×10^{-10} Ry per cell. The Brillouin zone (BZ) integration was performed using a $11 \times 11 \times 7$ Monkhorst-pack grid[61,62] generating 847 k-points in the irreducible part of the BZ.

2.6.2 Density of states and transport properties calculations

A Wannier function method was used for the extrapolation of electronic structure in the reciprocal space, as implemented in the *Wannier90* code and its *Boltzmann* module[63,64]. The initial Wannier projection were chosen to be Cr $3d$ and Si $3s$ and $3p$ orbitals. The Wannierized wavefunctions from the Cr $3d$ orbitals have ignorable difference from their atomic orbital counterparts, thus the Wannier functions can still be indexed by the $3d$ atomic orbital index. The density of states (DOS) was calculated by summing up the contribution from all bands and k-points from the Wannier extrapolation on a grid $50 \times 50 \times 30$. The temperature dependent chemical potential $\mu(T)$ estimated from experiments (see section 4.6.3), the calculated band structure and a constant carrier lifetime $\tau = 5.5 \times 10^{-15} s$ were used for the calculation of the transport properties using the linearized semi-classical Boltzmann equation[65]. The anisotropic values were obtained by using the following expressions:

$$\{\alpha,\rho\}_{\|c} = \{\alpha,\rho\}_{zz} \tag{2}$$

and

$$\{\alpha,\rho\}_{\perp c} = (\{\alpha,\rho\}_{xx} + \{\alpha,\rho\}_{yy})/2 \tag{3}$$

for both Seebeck coefficients and electrical resistivity along and perpendicular to the c-axis, the index x,y and z correspond the Cartesian axes. The anisotropic properties calculated in such way correspond to the case of an ideal single crystal, but due to the high texturation, they should also be comparable to our experimental measurements. COHP (Crystal Orbital Hamilton Population) curves which indicate energetic contributions of crystal orbitals between atoms, were calculated using the LOBSTER code[66–69].

2.6.3 Carrier concentration determination

As an important input for the transport calculation, the temperature dependent chemical potential $\mu(T)$ was determined from the carrier concentration n experimentally obtained from Hall measurements at room temperature, using the charge neutrality requirement $n_h(\mu,T) - n_e(\mu,T) = n$ with n_h and n_e the concentration of holes and electrons, respectively, which depend on the temperature T and the chemical potential μ according to the expression[70]:

$$n_h = \frac{1}{V}\int_{-\infty}^{\varepsilon_v} D(\varepsilon)\,(1 - f(\mu,\varepsilon,T))\,d\varepsilon \tag{4}$$

$$n_e = \frac{1}{V}\int_{\varepsilon_c}^{\infty} D(\varepsilon)\,f(\mu,\varepsilon,T)\,d\varepsilon \tag{5}$$

with ε_v and ε_c the energies of the valence band maximum (VBM) and the conduction band minimum (CBM), V the volume of the unit cell, $D(\varepsilon)$ the density of states obtained from the electronic structure calculation, and $f(\mu,\varepsilon,T)$ the Fermi-Dirac distribution function. The carrier concentration $n = 1 \times 10^{20}$ cm^{-3} was assumed to remain constant all over the temperature range. $\mu(T)$ was determined numerically using the equations (4) and (5). Since n is high, the calculated chemical potential was found below the valence band maximum at room temperature. It was shifted upward with increasing temperature but always found below VBM in the current assumption. A temperature dependent $\mu(T)$ was used for the calculations of the electrical resistivity and Seebeck coefficient. The above calculated carrier concentrations n_h and n_e with respect to temperature are shown in Figure SI 1.

3 Results and discussion

3.1 Synthesis of textured $CrSi_2$

A crucial step to obtain materials with high texturation using the magnetic slip casting process is the careful preparation of a stable slurry composed of single crystalline and mono-dispersed particles. Formation of aggregates would reduce the rotation movement of the particles in the dispersion and prevent the good alignment of their easy magnetization axis with the magnetic field. In addition, important aggregation of the particles may result in fast sedimentation of the slurry and the formation of a low-density green body with weak mechanical resistance. The particle size distribution is an important parameter that dictates the stability of the dispersion. Dispersions composed of particles with size less than 1 μm are expected to show higher stability as the effect of the Brownian force acting on the individual particles becomes preponderant over the gravitational attraction which tends to promotes their settlement. However, the random nature of the Brownian motion may also interfere with the proper alignment of small particles. Indeed, the magnitude of the magnetic torque T_m that rotates the individual particles upon application of a magnetic field B is given by the relation[42]:

$$T_m = -\frac{\Delta\chi V B^2}{2\mu_0} \times sin(2\theta) \tag{6}$$

where $\Delta\chi$ is the difference of diamagnetic susceptibilities between the hard and the easy magnetization axes, V is the volume of the particle, θ is the angle between the imposed magnetic field direction and the easy magnetization axis and μ_0 is the vacuum permeability. Relation (6) clearly shows that the magnitude of the magnetic torque is proportional to the particle volume. In practice, a good alignment of particles with size inferior to about 200 nm becomes challenging even with a magnetic field as high as 12 T due to

both lower T_m and increasing effect of the Brownian motion. Thus, a compromise on the particle size needs to be reached in order to allow both a good stability of the dispersion and a strong alignment of the particles. Considering the average diamagnetic constant $\chi_{dia} \approx$ -10^{-5} for $CrSi_2$ [71], powders with a medium value of the particle size distribution d_{50} between 1 μm and 200 nm are expected to give the best results.

The bulk $CrSi_2$ ingot used for the powder preparation was synthesized conventionally by arc-melting process. The XRD pattern of the as-cast ingot is shown in Figure 1a. All peaks could be indexed with the $CrSi_2$ structure which adopts the hexagonal $C40$ structure-type (space group $P6_222$, No. 180) shown in Figure 2a. Le Bail refinement gave lattice parameters a = 4.42724(6) Å and c = 6.36194(9) Å in agreement with literature data [72]. As shown in Figure 1b, the ingot was mostly composed of macroscopic crystals with size superior to 100 μm that were pulverized into powder using wet ball-milling. Figures 1c and d show a SEM image and the size distribution determined by DLS of the ball-milled $CrSi_2$ powder, respectively. The particle size distribution follows a log-normal law characterized by an average size and a standard deviation of 444 nm and 132 nm, respectively. A d_{50} value of 405 nm was determined from the cumulative frequency curve. The powder particles are fragments of large macroscopic crystals constituting the as-cast ingot and are thus considered as single crystalline. The present powder fulfills all the requirements stated above for the preparation of high-quality slurry for magnetic slip casting.

The electrostatic interactions between the particles in a dispersion is an other important parameter to take into account to prevent their aggregation and settlement. Increasing the repulsive electrostatic interactions between the particles was realized by adsorbing PEI at their surface. The zeta-potential, approximately corresponding to the surface electric charge of the particles, was increased from about -10 mV to -50 mV by adjusting the acidity of the solution with acetic acid. The viscosity of the slurry with a solid load of 20 wt.% was monitored for more than 2 hours and remained stable around 1.42 mPa s, confirming

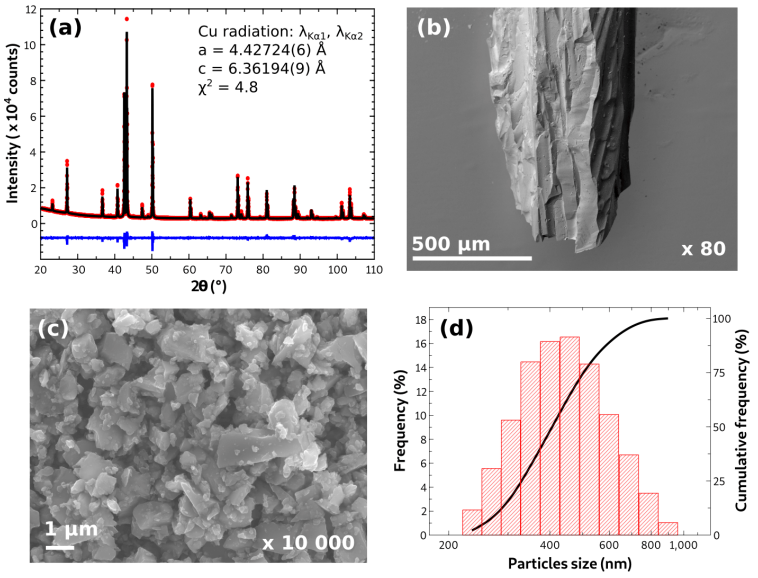

Figure 1: (a) Le Bail refined pattern and (b) SEM image of the as-casted $CrSi_2$ ingot showing that it is mostly composed of well-faceted macroscopic crystals, (c) SEM secondary electron images and (d) particle size distribution of the ball-milled $CrSi_2$ powder determined by DLS

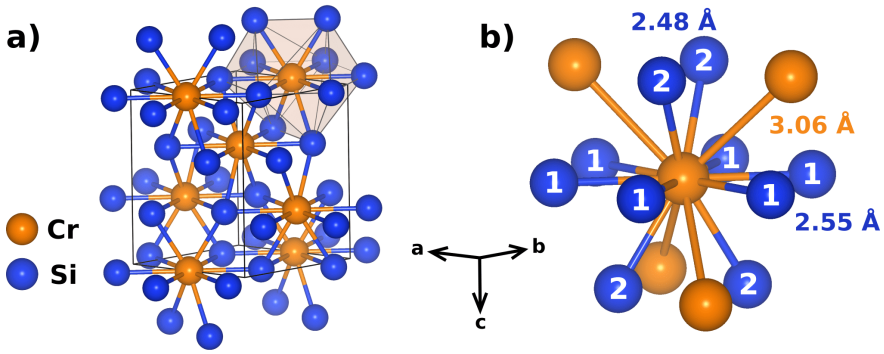

Figure 2: (a) Crystal structure of $CrSi_2$ and (b) coordination sphere around Cr composed of 10 Si and 4 Cr atoms

its good stability over time.

The slip-casting set-up is shown in Figure 3. After the slurry was poured, the mold was placed inside a superconducting magnet applying a 12 T static magnetic field. Depending on the desired texture direction, the magnetic field was applied either perpendicular or parallel to the slip casting direction. Indeed, the full characterization of TE materials requires samples shaped as thin pellets for thermal conductivity measurements with the

LFA method and bars for electric resistivity and Seebeck coefficient measurements using the 4-probe method. In the case of textured materials, the texture orientation needs to be the same, perpendicular to the pellet surface and parallel to the bar length. In the case of anisotropic materials, measurements of the TE properties along different texture directions may result in a highly overestimated *ZT*. Proper characterizations are usually achieved by cutting a thick densified pellet into smaller samples with shapes and dimensions well-adapted for the measurements. Instead, two different oriented samples with thickness of about 2 mm and complementary texture orientations were synthesized by setting the magnetic field direction vertically (sample $CrSi_2$-v) or horizontally (sample $CrSi_2$-h). A reference sample with random orientation ($CrSi_2$-r) was also prepared using the same process but without magnetic field. Within 8 hours, the solvent of the dispersion went entirely through the membrane into the porous support leaving green bodies with relative densities of about 55 %. In those conditions, the green bodies did not show enough mechanically stability to withstand the uniaxial pressure applied during sintering. Therefore, they were first consolidated via CIP technique to a relative density $\approx$ 65 % while preventing degradation of the texturation (see Figure SI 2). Finally, the green bodies were sintered via SPS technique into pellets with relative density of 98 % and 96 % for random and oriented samples, respectively. Despite identical sintering conditions for all the samples, crystallographic orientations of the grains in the green bodies may affect significantly the surface energy and therefore the densification mechanisms resulting in slightly different densities.

The powder XRD patterns of the sintered random and oriented pellets shown in Figure 4a were well indexed with the $CrSi_2$ structure. SEM back-scattered electron image and EDS analyses of the $CrSi_2$-v sample surface are shown in Figure 4b and Figure SI 3, confirming that $CrSi_2$ is the main phase. However, SEM analyses also revealed some CrSi impurity visible as light gray spots of about 1 μm for all the samples. These impurities representing a negligible phase fraction of the samples were no detected on the XRD patterns. One

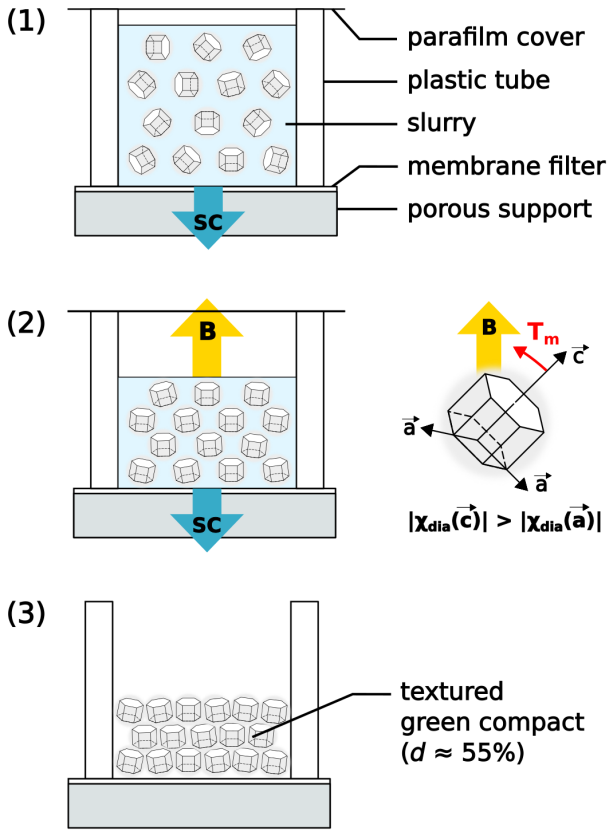

Figure 3: Description of the texturation process in 3 steps: (1) the slurry is poured in the slip casting (blue arrow) set-up and the solvent starts to be slowly drained through the membrane inside the porous support (2) the particles in the slurry are being aligned along their easy magnetization axis by application of a vertical 12 T magnetic field (yellow arrow) inducing a magnetic torque (3) a textured green body is obtained after all the solvent had been removed

possible explanation to the presence of CrSi is probably the reaction of residual dispersant at the surface of the particles with the $CrSi_2$ matrix during sintering. However, such a small amount of impurity was not expected to be detrimental to the TE properties and these samples were used for TE measurements. The XRD patterns of $CrSi_2$-v and $CrSi_2$-h shown in Figure 4a indicate large discrepancies of the peak intensities compared to $CrSi_2$-r. This is attributed to large crystallographic texturations. In the case of $CrSi_2$-v, which was synthesized with the magnetic field direction perpendicular to the pellet surface, only the diffraction peaks 0003 and 0006, using the 4-index *hkil* Miller-Bravais notation, are visible at $2\theta \sim 42^\circ$ and $\sim 96^\circ$, respectively. This indicates that the *c*-axis of $CrSi_2$ is the

easy magnetization axis and thus the diamagnetic constant $|\chi_c|$ is inferior to $|\chi_{a,b}|$. On the contrary, the pattern of $CrSi_2$-h shows largely reduced $000l$ peaks compared for example to $11\bar{2}0$ at $2\theta \sim 40°$ for $CrSi_2$-r. These results clearly indicate that the present process is an efficient route to synthesize highly textured $CrSi_2$ samples with good purity.

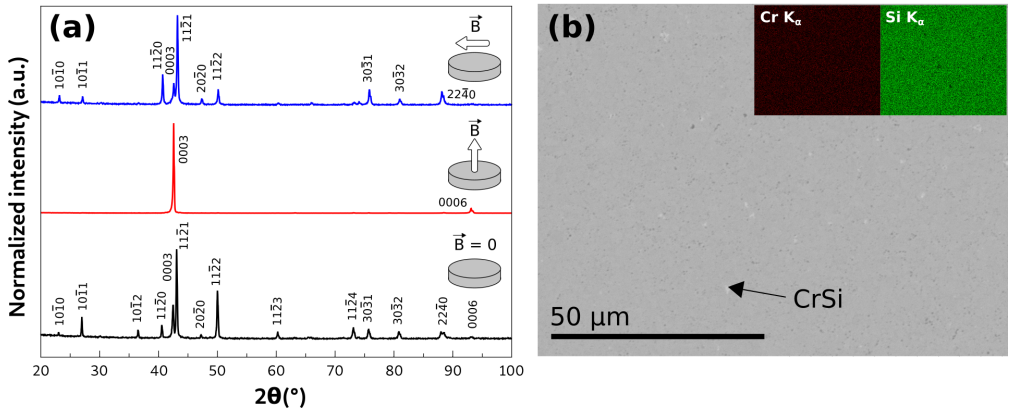

Figure 4: (a) XRD patterns of $CrSi_2$-r (black), $CrSi_2$-v (red) and $CrSi_2$-h (blue) sintered samples (b) SEM back-scattered electron image of the sample's surface of $CrSi_2$-v with corresponding EDS elementary maps

3.2 Quantitative texture analyses

In order to unambiguously study the effect of texturation on the TE properties and to make meaningful comparisons between different synthesis methods of texturation, it is essential to determine quantitatively the orientation and the strength of the main alignment components of the textures. In the present case, this was realized using both complementary EBSD and XRD techniques. EBSD maps of the $CrSi_2$ samples are shown in Figure 5. The black areas correspond to unindexed zones which are mostly attributed to surface imperfections consecutive to polishing and, to a lesser extent, residual porosities and CrSi secondary phase. The crystallite orientation map and inverse pole figure (IPF) with homogeneous orientation density of 1 mrd (multiple random distribution) confirm the absence of texturation for $CrSi_2$-r. In the case of the oriented samples, visual inspection of the maps clearly reveals the presence of textures with the majority of the crystallites showing a $\{000l\}$ and a $\{hki0\}$ orientations for $CrSi_2$-v and $CrSi_2$-h, respectively. The IPF of $CrSi_2$-v

shows an important *c*-axis texturation of about 20 mrd along the X direction of the sample surface. A similar *c*-axis texture of about 20 mrd is also found for $CrSi_2$-h but along the Y direction that is parallel to the sample surface. In both cases, the main alignment component is aligned with the magnetic field direction applied during slip casting. The IPF along the Y and Z directions of $CrSi_2$-v and the X and Z directions of $CrSi_2$-h reveals that the *a*-axis of the crystallites is randomly oriented in the plane perpendicular to the easy-axis direction resulting in a fiber texture symmetry. This suggests that the dispersed particles in the slurry remain free to rotate around the *c*-axis when the magnetic field is applied. Such a fiber texture symmetry is common for materials synthesized by this process and can be found, for example, in hexagonal Al_2O_3[73] and $LiCoO_2$[74].

XRD measurements were performed as a complementary texture characterization presenting the advantage to analyze a larger volume fraction of the sample. The analyses consisted in measuring several θ-2θ scans at different tilting angles χ and azimuthal rotation ϕ using a X-ray diffractometer equipped with χ-ϕ attachment as schematized in Figure 6a. Figures 6b and 6c show the square root of the diffracted intensities for $CrSi_2$-r and $CrSi_2$-v, respectively, at different χ angles. Measurements with different ϕ rotation were unnecessary because of the texture symmetry of these samples evidenced by EBSD analyses. In the opposite case of $CrSi_2$-h, the texture axis is parallel to the sample surface and the relative diffracted intensities are thus expected to vary with ϕ rotation. Because of the large number of measured patterns for $CrSi_2$-h (162 in total) the square root of the diffracted intensities is only shown in Figure 6d for fixed $\chi = 25^\circ$. Diffraction data for $\chi \leqslant 40^\circ$ were not taken into account in the analysis because of the defocusing effect which provokes a large broadening of the peaks at higher angles. The analyses of the crystal structure and texturation of the samples were performed simultaneously by fitting the whole collection of diffraction patterns using conventional Rietveld method combined with a refinement of the orientation distribution (OD) with the algorithm E-WIMV[75,76] as implemented in the

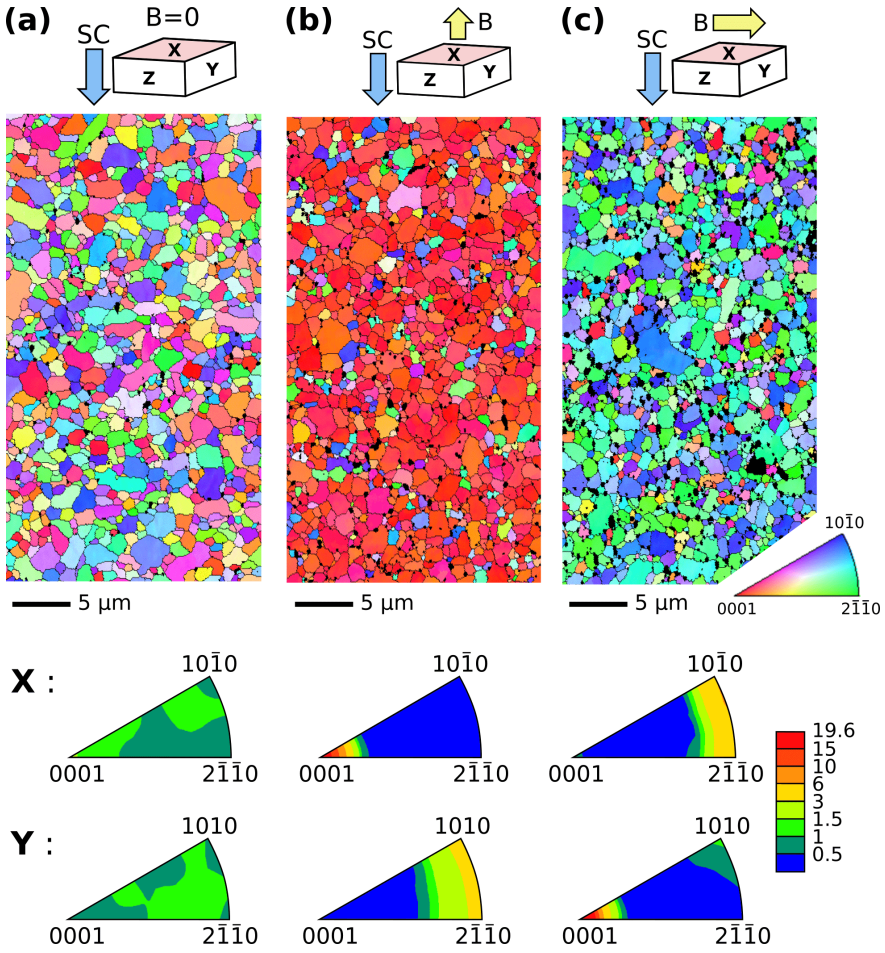

Figure 5: EBSD maps of the surface of (a) $CrSi_2$-r, (b) $CrSi_2$-v and (c) $CrSi_2$-h. with the corresponding IPF

software MAUD[56]. In the initial step of this procedure, a first refinement of the OD was made from the integrated intensities determined by Le Bail refinement. The obtained OD was then introduced in the Rietveld algorithm and the initial structural model was refined. The refined set of structural parameters was then used for OD refinement and so on until the refinement procedure converged. Conventional R_{wp}, R_{exp} and χ^2 profile reliability values were used to assess the conformity of the Rietveld refinement of the whole data set. Similarly, the Rietveld-like R_b and R_w reliability values were used to assess the quality of the OD refinement[76]. A selection of refined diffraction patterns for $CrSi_2$-h and the refined structural parameters for all the samples are shown in Figure 7a and **Table 1**, respectively. A selection of refined diffraction patterns for $CrSi_2$-r and $CrSi_2$-v can be found in Figures

SI 4 and SI 5. The refined OD were used to calculate the IPF for all the samples shown in Figure 7b. In addition to give precious texture information, this method has the advantage to enable crystal structure refinement of the samples used for TE measurements despite the strong effect of the texture on the diffracted intensities.

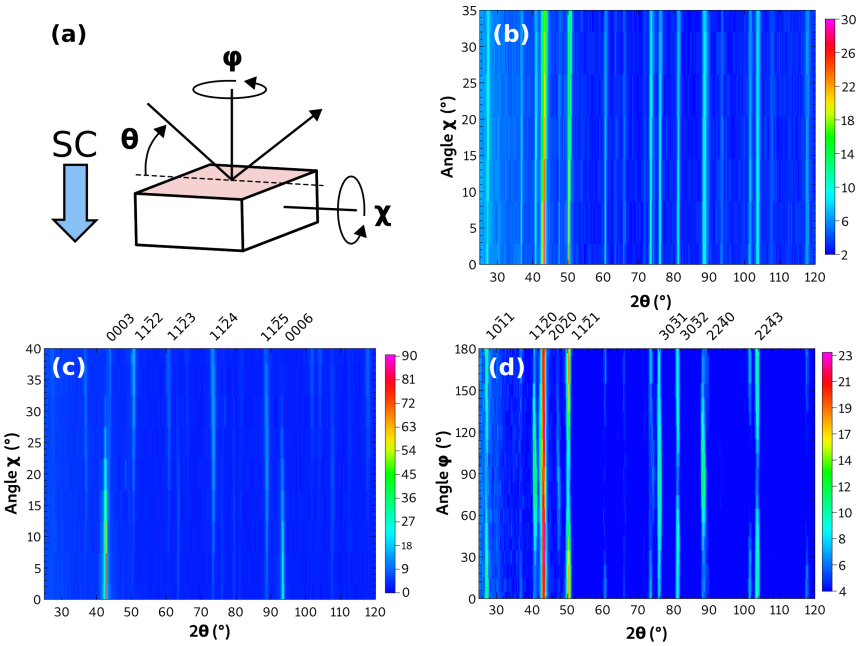

Figure 6: (a) Schematic representation of the XRD geometry used for texture analyses. 2D maps showing the square root of the diffracted intensities for (b) $CrSi_2$-r with $0^\circ \leqslant \chi \leqslant 35^\circ$, (c) $CrSi_2$-v with with $0^\circ \leqslant \chi \leqslant 40^\circ$ and (d) $CrSi_2$-h with with $0^\circ \leqslant \phi \leqslant 180^\circ$ and $\chi = 25^\circ$

The refined lattice and structural parameters are similar for all the samples with $a \approx 4.43$ Å, $c \approx 6.36$ Åand $x \approx 0.166$ for the position coordinate of Si on the 6*j* Wickoff site. These values correspond well to those determined above for the as-cast ingot and those reported in the literature[72]. High profile reliability values were obtained due to the large number of data patterns used for the refinement but also to the difficulty to take into account the asymmetry of the very intense 0003 peak at low χ angles in the patterns of $CrSi_2$-v. However, the OD *R*-factors show acceptable values especially in the case of the present sample showing strong texturation strength. In the case of randomly oriented

$CrSi_2$-r shown in Figure 6b, no visible variation of the relative peak intensities was noticed upon increasing of χ angle. In agreement with EBSD analysis, the calculated IPF show no significant texturation. The XRD patterns of $CrSi_2$-v and $CrSi_2$-h reveal clear variation of the relative intensity of the peaks with χ and ϕ angles, respectively. In the case of $CrSi_2$-v (Figure 6c), the intense 0003 reflection at $\chi = 0^\circ$ rapidly decreases to become weak at $\chi = 25^\circ$. The $11\bar{2}4$ reflection at $2\theta \sim 74^\circ$, with weak intensity at $\chi = 0^\circ$, becomes relatively intense at $\chi = 30^\circ$. It corresponds well to the angle of 27.6° that forms between the normal of the families of Miller planes $11\bar{2}4$ and 0003 and thus where they are expected to be in diffraction condition in the case of a perfectly oriented sample. In the case of $CrSi_2$-h (Figure 6d), were the crystallites are predominantly oriented with their *c*-axis along Y direction, the Bragg intensities are strongly varying with the ϕ rotation. For example, the $11\bar{2}0$ reflection at $2\theta \sim 40^\circ$ is the most intense reflection when the sample *c*-axis texture direction is parallel with the diffraction plane (at $\phi = 90^\circ$) than perpendicular (at $\phi = 0^\circ$ or 180°). In the opposite, other Bragg reflections such as $30\bar{3}2$ at $2\theta \sim 81^\circ$ or $22\bar{4}3$ at $2\theta \sim 104^\circ$ have their maximum intensities at $\phi = 0^\circ \equiv 180^\circ$. Calculated IPF for $CrSi_2$-v and $CrSi_2$-h show high *c*-axis texture along the X and Y directions, respectively, in agreement with EBSD results. The maximum orientation densities of about 10 mrd in both cases are about twice smaller than those determined by EBSD. The discrepancy between the two techniques can be attributed to the limited number of analyzed grains by EBSD but also because of the imperfect fitting of the XRD diffraction patterns. However, both techniques agreed that the easy axis texture has a high and comparable orientation strength regardless of the magnetic field direction. This is of uttermost importance in order to properly compare the directional TE properties and obtain reliable estimation of *ZT*.

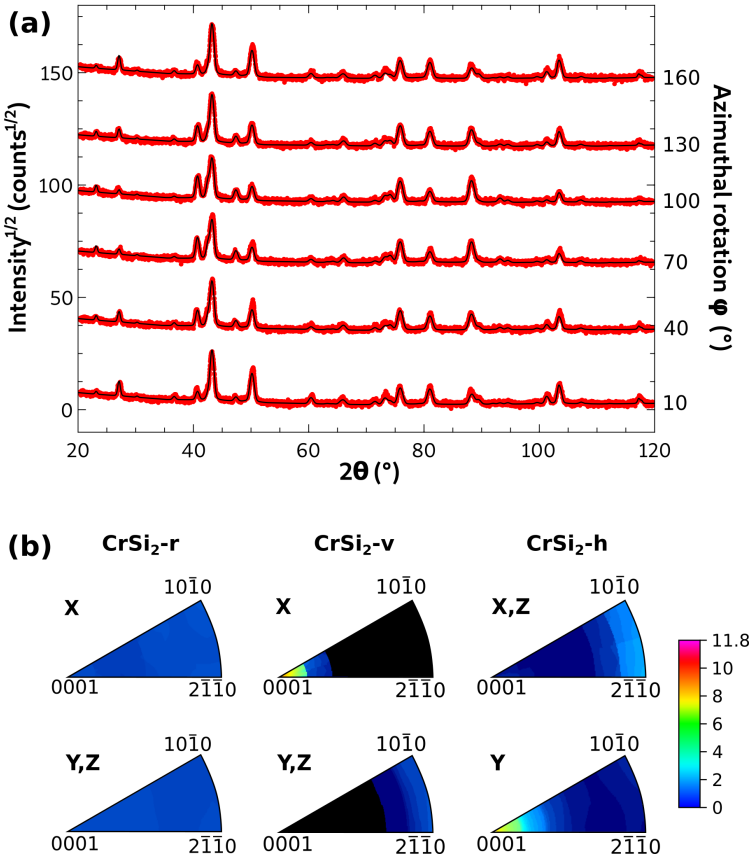

Figure 7: (a) Selection of Rietveld refined XRD patterns of $CrSi_2$-h measured at different ϕ rotations and at $\chi = 20°$ (b) IPF calculated from the combined Rietveld and OD refinements of the XRD patterns

3.3 Thermoelectric property measurements

The Seebeck coefficient, electrical resistivity and thermal conductivity of the magnetically oriented bulk $CrSi_2$ samples were measured over the 300-800 K temperature range, in order to evaluate their anisotropy. As shown in Figure 8, the thermal conductivity parallel ($\kappa_{\parallel c}$) and perpendicular ($\kappa_{\perp c}$) to the *c*-axis texture were measured on the pellet-shaped $CrSi_2$-v and $CrSi_2$-h samples, respectively. The measured thermal conductivities shown in Figure 9a reveal a moderate anisotropy. At 323 K for instance, $\kappa_{\parallel c}$ is higher than $\kappa_{\perp c}$ with values of 13.5 and 10.9 W m^{-1} K^{-1}, respectively. It corresponds to a $\kappa_{\parallel c}/\kappa_{\perp c}$ ratio of 1.25 that remains constant up to the highest measured temperature of 773 K. This ratio is lower than for single crystals with reported value of 1.5[34]. This must be due the lower

Table 1: Structural parameters and R-values obtained by the combined structural and OD refinement of $CrSi_2$-r, $CrSi_2$-v and $CrSi_2$-h XRD patterns

	$CrSi_2$-r	$CrSi_2$-v	$CrSi_2$-h
Number patterns	8	9	162
a (Å)	4.43015(5)	4.42850(8)	4.42996(5)
c (Å)	6.36161(8)	6.36234(4)	6.36117(7)
Volume (Å^3)	108.12	107.67	108.11
	Cr at 1/2, 0, 0 (Wickoff pos. 3d)		
B_{iso} (Å^2)	0.25(2)	0.15(1)	0.31(2)
	Si at x, -x, 1/3 (Wickoff pos. 6j)		
x	0.1662(4)	0.1669(5)	0.1661(5)
B_{iso} (Å^2)	0.29(2)	0.48(2)	0.37(2)
	Profil R-factors		
R_{wp} (%)	23.3	31.0	29.85
R_{exp} (%)	19.6	17.9	20.0
χ^2	1.4	3.0	2.3
	OD R-factors		
R_w (%)	4.6	13.4	14.5
R_b (%)	7.6	15.4	16.3

orientation strength in the textured polycrystalline sample as well as the presence of grain boundaries participating in the diffusion of heat-carrying phonons. Randomly textured $CrSi_2$-r logically shows intermediate values with κ of 11.9 W m^{-1} K^{-1} at 323 K.

The electronic contribution to the thermal conductivity was estimated using the Wiedemann-Franz law to be around 0.60±0.15 W m^{-1} K^{-1} for all the samples. This means that the difference of total thermal conductivities along the different crystallographic directions is mostly due to different lattice thermal conductivities, *i.e.*, propagation of heat-carrying phonons by the lattice. The present thermal conductivities are slightly higher than some reported κ values for polycrystalline $CrSi_2$ which are generally close to 10 W m^{-1} K^{-1} at the same temperature[77]. This is attributed to the higher relative density of our samples

($>$ 96 %) compared to samples from the literature which usually show relative densities in the range of 90 - 92 %. In the present case, higher densities could be achieved by increasing significantly the sintering temperature to 1573 K using a pyrometer for temperature control instead of a conventional K-type thermocouple limited to a maximum temperature of 1273 K. Note that it has been shown both experimentally[78,79] and theoretically[80] that κ for $CrSi_2$ is relatively high mainly owing to the high lattice thermal conductivity part, which is responsible for over 90 % of κ.

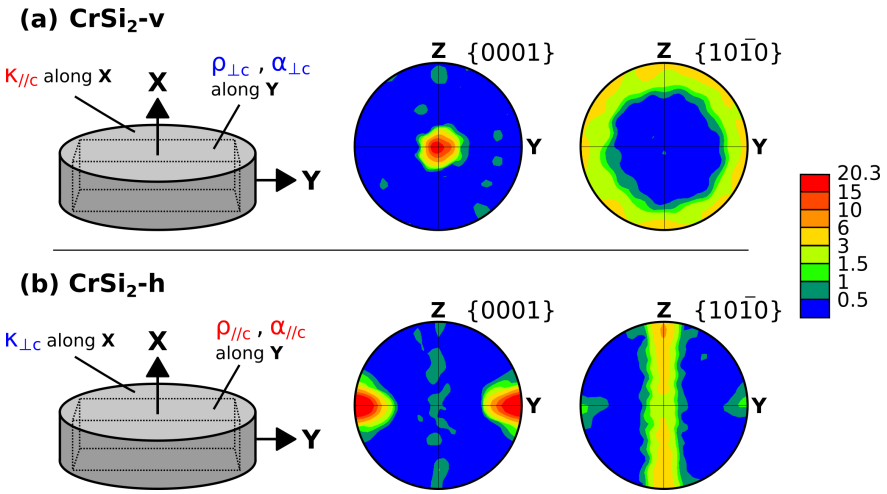

Figure 8: Scheme showing how the pellets of (a) $CrSi_2$-v and (b) $CrSi_2$-h were cut and measured for directional TE measurements and the corresponding {0001} and {10$\bar{1}$0} EBSD pole figures

For the measurement of electrical transport properties $\|c$ and $\perp c$, the pellets were cut into bars along the directions shown in Figure 8. The Seebeck coefficients and electrical resistivities parallel ($\alpha_{\|c}$ and $\rho_{\|c}$) and perpendicular ($\alpha_{\perp c}$ and $\rho_{\perp c}$) to the c-axis texture direction were measured on the samples $CrSi_2$-h and $CrSi_2$-v, respectively. The temperature dependence of α for all samples follows the same general tendency, *i.e.* increases from 327 K to their maximum values around 625 - 650 K and then decreases up to the highest measured temperature (Figure 9b). However, the magnitude of α strongly varies with regards to the crystallographic orientation. Indeed, $\alpha_{\|c}$ reaches 198 μV K^{-1} at 627

K while $\alpha_{\perp c}$ is only 134 μV K^{-1} at the same temperature which results in a $\alpha_{\parallel c}/\alpha_{\perp c}$ ratio of 1.5. All these values compare very well with corresponding single crystal data from the literature reporting $\alpha_{\parallel c}$ and $\alpha_{\perp c}$ of about 200 and 135 μV K^{-1}, respectively[34].

The electrical resistivity (Figure 9c) exhibits less anisotropic behavior compared to the Seebeck coefficient. At about 650 K where the lowest electrical resistivities are measured, a $\rho_{\parallel c}/\rho_{\perp c}$ anisotropy of about 0.75 is observed with $\rho_{\parallel c}$ = 15 $\mu\Omega$ m and $\rho_{\perp c}$ = 20 $\mu\Omega$ m. Measurements previously reported on single crystal confirms the lower ρ along [0001] than [10$\bar{1}$0] but with a significantly larger anisotropy with a $\rho_{[0001]}/\rho_{[10\bar{1}0]}$ ratio of 0.5 at 650 K[34,81]. Note that a quantitative comparison of electronic resistivities between polycrystalline samples and single crystals is in turn difficult to establish due to the presence of grain boundaries in the former. Surprisingly, electrical resistivity of $CrSi_2$-r is consistently lower on the whole temperature range than for both textured samples whereas intermediate values would be expected. Hall measurement performed on the non-textured sample $CrSi_2$-r gives a charge carrier concentration $n = 9 \times 10^{20}$ cm^{-3} and an electron mobility μ = 7 cm^2 V^{-1} s^{-1} at 298 K which are consistent with literature data[21]. The lower resistivity of $CrSi_2$-r is not attributed to different charge carrier concentrations among the sample as they were synthesized from the same powder batch and using the same process conditions. Unfortunately, this could not be verified experimentally since Hall measurements of non-isotopic materials require the determination of the galvanomagnetic tensor entering the Hall equation[82] which cannot be accurately determined on textured samples due to the imperfect crystallographic orientations[83]. The lower electrical resistivity of $CrSi_2$-r is more likely due to its higher density (98 %) compared to that of the textured samples (96 %).

It is well known that α and ρ are interdependent in TE materials which makes large improvement of the power factor (*PF*) challenging. Interestingly, in the case of $CrSi_2$, both α and ρ show the best TE properties along the *c*-axis. As a result, the magnetically oriented

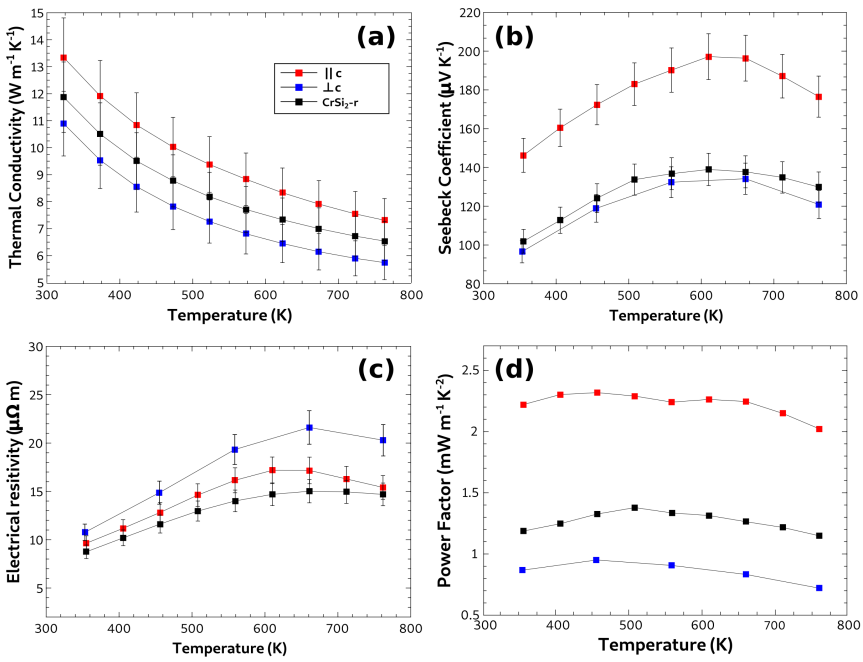

Figure 9: High temperature thermoelectric properties of $CrSi_2$ parallel to the *c*-axis orientation (red), perpendicular to the *c*-axis orientation (blue), for random orientation (black) and for the reference sample (white): (a) thermal conductivity, (b) Seebeck coefficient, (c) electrical conductivity and (d) power factor. The estimated relative uncertainty is 11 %, 8 % and 6 % for the thermal conductivity, electrical resistivity and Seebeck coefficient, respectively[84].

samples show that $PF_{\|c}$ is much higher than $PF_{\perp c}$ with values superior to 2 mW m^{-1} K^{-2} over the whole temperature range measured as shown in Figure 9d. From the TE properties measured along the different texture direction on the samples $CrSi_2$-v and $CrSi_2$-h, it is possible to calculate an estimated directional *ZT* (**Figure 10**). It is worth to notice that because the thermal conductivity and electronic properties measured $\|c$ and $\perp c$ were not performed on the same samples, the *ZT* values presented here can only be taken as an estimation. Nevertheless, $CrSi_2$-r have a maximum *ZT* of 0.13 at 773 K which is in good agreement with literature data for polycrystalline $CrSi_2$[20]. Thanks to the larger *PF* and despite a higher thermal conductivity, $ZT_{\|c}$ is much higher than $ZT_{\perp c}$ on the whole temperature range reaching a maximum of 0.20 at 773 K. This represents a 50 % improvement of *ZT* compared to the randomly oriented sample. A prove of the high quality of the texturation is that the present estimated $ZT_{\|c}$ is very similar to the *ZT* along the *c*-axis reported for

single crystals (Figure 10)[34]. This demonstrates that slip casting under a magnetic field is promising as a texturation processing route to fully take advantage of thermoelectric materials with anisotropically decoupled electrical transport properties.

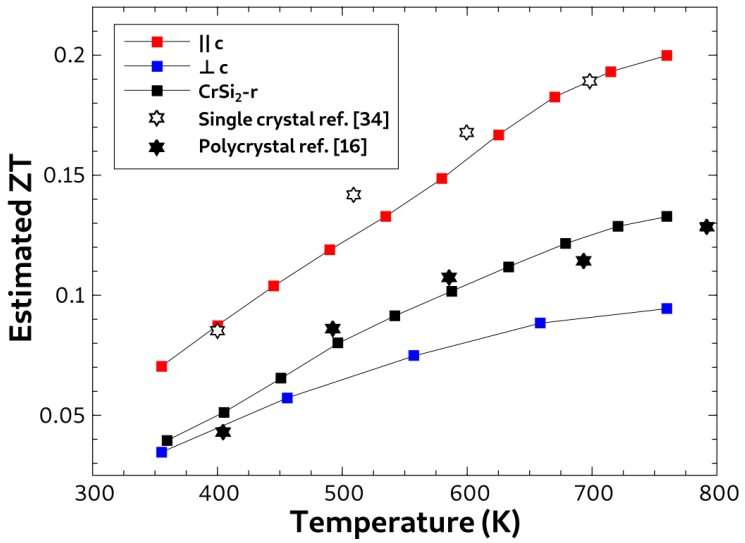

Figure 10: Estimated *ZT* of $CrSi_2$ parallel to the *c*-axis orientation (red), perpendicular to the *c*-axis orientation (blue), for random orientation (black) and for the reference sample (white). Literature *ZT* values measured on single crystalline[34] and polycrystalline[16] samples are shown with empty and filled star symbols, respectively.

3.4 Theoretical calculations

DFT band structure calculations and electronic transport property computations were performed on bulk $CrSi_2$ in order to rationalize the anisotropy of the Seebeck coefficient and the electrical resistivity experimentally observed for the magnetically *c*-axis oriented samples (see the experimental section for computational details). The calculated band structure and DOS are shown in Figures 11a and b, respectively. The band structure reveals semiconducting properties with an indirect band gap of 0.35 eV between a valence-band maximum at *L* and a conduction band minimum at *M*. The smallest value for a direct band gap is 0.52 eV at *L* (see the first Brillouin zone (BZ) in Figure SI 6 for the labeling of the symmetry points and symmetry lines). These band gap values are in a good

agreement with those computed previously[77,81,85] and the experimentally measured optical value[86,87].

As previously noticed, the electronic structure of $CrSi_2$ is quite complicated due to its specific atomic arrangement[77,81,85] with both flat and dispersive bands computed in almost all directions of the BZ (Figure 11a). Indeed, the crystal structure of $CrSi_2$ contains individual hexagonal $CrSi_2$ layers stacking along the *c*-axis which are interrelated via non-primitive translations ($t = c/3$ and $2c/3$) (Figure 2a). Such a stacking implies that each Si and Cr atom is surrounded by a well-defined polyhedron made of ten nearest neighbors with comparable Cr-Si and Si-Si bond distances. In addition to six planar neighbors (Si1) situated at 2.55 Å apart in the *a*,*b*-plane, each Cr is tetrahedrally coordinated along the *c*-axis with four interplanar neighbors (Si2) positioned at a shorter distance of 2.47 Å. Additionally, somewhat further apart from the central Cr atom, 4 Cr atoms form a distorted tetrahedral at a distance of about 3.06 Å which reflects some bonding interaction (see Figure 2b for the Cr atomic surrounding). Atom-projected DOS curves in the [-5, 5] eV range (not shown here) indicate that the valence-band and conduction-band states originate from Cr states hybridized with Si states, whereas the states around the band gap show a predominantly Cr 3d character. This demonstrates strong covalent interactions in the structure. With shorter Cr-Si bonding distances and some Cr-Cr interaction along the *c*-axis, stronger covalency is expected than in the *a*,*b*-plane and consequently some anisotropy in the electronic transport properties should occur. This stronger covalency along the *c*-axis is demonstrated by the atomic orbital-projected DOS which indicate higher dispersion for the Cr d_{z^2} one (Figure 11b).

The electronic transport properties, namely the Seebeck coefficient and the electrical resistivity were computed as function of the temperature both parallel and perpendicular to the *c*-axis. There are compared to experiments in Figure 12. A good quantitative agree-

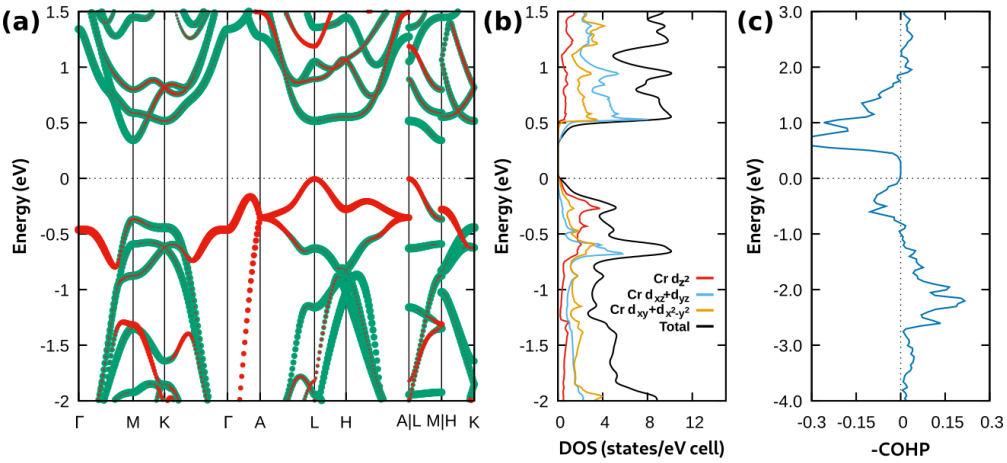

Figure 11: (a) calculated band-structure of $CrSi_2$ with the contribution of the $3d_{z^2}$ orbital in red and other 3d orbitals in green. (b) corresponding total and projected density of states (DOS). The cartesian axes z, and x and y are along the c-axis and in the a,b-plane, respectively. (c) Calculated COHP for Cr-Cr interactions in $CrSi_2$.

ment between theory and experiments is observed overall for the Seebeck coefficient. The gradual increase with the temperature is well reproduced up to 600 K both for $\alpha_{\|c}$ and $\alpha_{\perp c}$. On the other hand, the rapid decrease of the Seebeck coefficient observed experimentally above 600 K is not predicted by the calculations. Note that in our calculations, the number of n-type carriers is always far less than the p-type holes due to the high extrinsic p-type carrier concentration, and therefore the intrinsic bipolar excitation effect should be unsignificant. We think that a possible reason for the decrease of the thermopower beyond 600 K for both $\alpha_{\|c}$ and $\alpha_{\perp c}$ may be extrinsic excitations occurring at high temperature rather than bipolar diffusion of carriers. Interestingly, the large anisotropy $\alpha_{\|c}/\alpha_{\perp c}$ of the Seebeck coefficient evidenced experimentally is theoretically confirmed. This anisotropy needs to be rationalized. Indeed, in a single band model without competing scattering events, the Seebeck coefficient is expected to be isotropic even if the electrons may have a different effective mass along different crystallographic directions[88,89]. In the case of $CrSi_2$, the band structure shows a band along the $\Gamma \rightarrow A$ symmetry line (Δ) (corresponding to the c-direction in the real space) with the maximum in the vicinity of A that is only 0.15 eV below the maximum at L of the valence band along the $A \rightarrow L$ symmetry direction (R)

(corresponding to the *a*,*b*-plane in the real space). The anisotropy of the Seebeck coefficient in $CrSi_2$ may thus originate from a multi-band conduction with a different electron mobility ratio along the *c*-axis and the *a*,*b*-plane. In a two-band model, the combined Seebeck coefficient α_{tot} is the electron mobility m^* weight average of the contributions α_R and α_Δ of the bands *R* and Δ, respectively, along a specific crystallographic direction in the reciprocal space[90,91]:

$$\alpha_{tot} = \frac{N_R \beta \alpha_R + N_\Delta \alpha_\Delta}{N_R \beta + N_\Delta} \tag{7}$$

with N_R and N_Δ the multiplicity of the bands and β the mobility ratio between the two bands along this crystallographic direction:

$$\beta = \frac{m_R^*}{m_\Delta^*} \tag{8}$$

The effective masses and multiplicities of the two bands *R* and Δ calculated form the band structure calculations are given in Table 2.

Table 2: Multiplicities and calculated effective masses along *c* and in the *a*,*b* plane for the band *R* and Δ of $CrSi_2$

	Band *R*	Band Δ
m_c^*	0.88	0.56
$m_{a,b}^*$	1.37	3.10
N	3	2

The Seebeck contribution of each band with respect to the temperature was calculated using the parabolic band model and an estimated chemical potential $\mu(T)$ (see the experimental section for details) using the equation:

$$\alpha(T) = \frac{1}{eT} \frac{\int \varepsilon^{3/2+\eta}(\varepsilon - \mu)(-\frac{\partial f}{\partial \varepsilon}) d\varepsilon}{\int \varepsilon^{3/2+\eta}(-\frac{\partial f}{\partial \varepsilon}) d\varepsilon} \tag{9}$$

with η = -1/2 for acoustic phonon scattering. The Seebeck coefficient values obtained from equation (7) by introducing $\alpha(T)$ calculated from eq. (9) and the parameters given in Table 2 for each band successfully predict qualitatively the large anisotropy measured experimentally with a $\alpha_{\parallel c}/\alpha_{\perp c}$ ratio of about 1.4 all over the 300 - 800 K temperature range (Figure SI 7a). This result shows that the anisotropy in Seebeck must come from the difference in mobility ratio between the hole pocket participating in the electrical conduction. The contribution from the pocket Δ is large and leads to a much enhanced Seebeck coefficient along the c-axis. Note that using a somewhat more sophisticated approach derived from the microscopic electronic model for multi-valleyed materials with parabolic bands proposed by Bies *et al.*[89] modified for non-degenerate bands, leads to a more quantitative agreement (compare Figure 12a and Figure SI 7b).

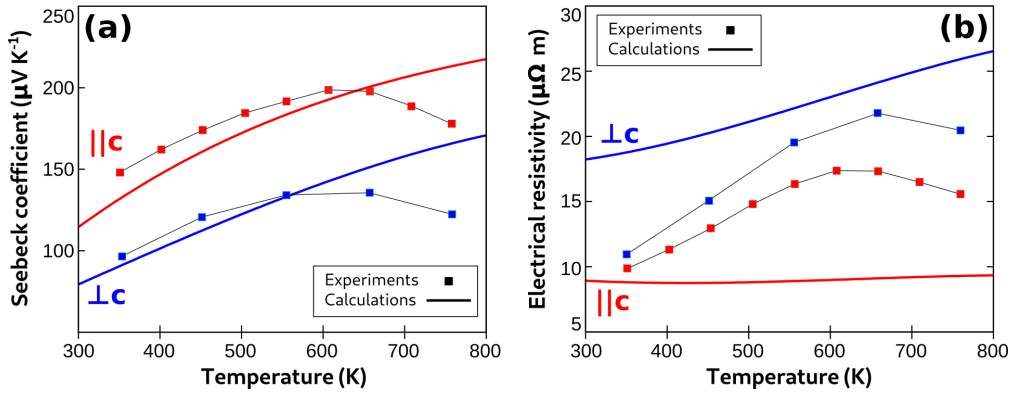

Figure 12: Calculated (solid line) and experimental (signs) Seebeck coefficient (a) and electrical resistivity (b) for $CrSi_2$. Transport properties along the c-axis and in the a,b-plane are in blue and red, respectively.

The electrical resistivity behavior (especially $\rho_{\perp c}$) shown in Figure 12b indicates a degenerated-semiconductor character for $CrSi_2$ because of the high hole concentration that remains stable over the whole 300 - 800 K temperature range (Figure SI 1). However, it largely deviates quantitatively from the experimental data as a result of the constant carrier lifetime approximation used for the calculations, within which the temperature dependence of the scattering time as the result of lattice thermal vibration is not considered

at all. Nonetheless, the anisotropy is correctly reproduced by the calculations with the highest electrical resistivity computed along the *c*-axis. Note that both *R* and Δ bands (Table 2) show small effective masses m_c^* with respect to $m_{a,b}^*$, and therefore high hole mobility along the *c*-axis. This is in agreement with the Si-Si, Si-Cr and Cr-Cr covalent character stronger along the *c*-axis than in the *a*,*b*-plane which leads to more dispersive bands favoring smaller effective masses. In particular, the strong Cr-Cr interaction along the *c*-axis is confirmed by an analysis of its corresponding COHP curve (Figure 11c) and its integrated-ICOHP value (0.364 Ry/cell) with respect to that of the very weak Cr-Cr interaction in the *a*,*b*-plane (-ICOHP = 0.036 Ry/cell). In agreement with a previous report[77], the Cr-Cr COHP curve along the *c*-axis features quite substantially Cr antibonding states below the Fermi level. This indicates that (i) the bonding situation in $CrSi_2$ is not fully optimized, and (ii) these antibonding states play a major role in determining the electrical transport properties.

4 Conclusion

In this paper, an original synthesis method to obtained good quality and highly textured polycrystalline $CrSi_2$ material is presented. It consists in applying a strong magnetic field during the slip casting of a $CrSi_2$ suspension to orient the particles along their easy magnetization. Both EBSD and XRD analyses indicated a strong fiber texture symmetry of the sintered pellets with maximum {0001} texture densities > 10 mrd parallel to the magnetic field direction. The TE properties were measured parallel and perpendicular to the texture direction. The thermal conductivity showed a moderate anisotropy with a $\kappa_{\parallel c}/\kappa_{\perp c}$ ratio of 1.25 at 773 K. Surprisingly, the Seebeck coefficient showed a much larger anisotropy with $\alpha_{\parallel c}/\alpha_{\perp c} \sim 1.5$ and $\alpha_{\parallel c}$ reaching a maximum of 198 μV K^{-1} at 650 K. The electrical resistivity was also lower $\parallel c$ which results in largely improved $PF_{\parallel c}$ of about 2 mW m^{-1} K^{-2} on the whole temperature range. This is 100 % and 60 % higher than $PF_{\perp c}$ and PF of a randomly oriented sample, respectively. DFT calculations revealed that the high $\alpha_{\parallel c}$, and

consequently $PF_{\|c}$, originate from a two-band conduction and the large presence of the Cr d_{z^2} states near the valence band maximum in $CrSi_2$. The measurements of the TE properties along the different texture directions of two oriented samples enable the estimation of the directional ZT. A maximum $ZT_{\|c}$ of 0.2 at 773 K was estimated which is consistent with values reported for single crystal and represents a 50 % improvement compared to untextured polycrystalline $CrSi_2$. The present work clearly shows that texturation can be advantageously used to improved the TE properties of bulk polycrystalline thermoelectric silicides that are promising materials for industrial applications. Additional studies are currently being undertaken to increase even more the industrial potential of this process, for example, by increasing the dimension of the samples that can be synthesized (without inducing texture heterogeneity) but also by reducing the magnetic field strength required for the particles orientation (ideally using permanent magnets). Finally, the approach used here for silicides can certainly also be applied to other high performance materials showing large anisotropy of their TE properties such as higher manganese silicides or SnSe.

Acknowledgements

This work was supported by the Japan Society for the Promotion of Science (JSPS) (grants number PE19749). TM acknowledges the funding from JST-Mirai (JPMJMI19A1).

Supporting Information

Supporting Information Available: Calculated carrier concentration as a function of temperature, XRD patterns of the samples $CrSi_2$-v, $CrSi_2$-h and $CrSi_2$-r after CIP treatment, SEM-EDS spectrum of the $CrSi_2$ phase, Rietveld refined XRD patterns of $CrSi_2$-v measured at different χ rotations and at $\phi = 0°$, Rietveld refined XRD patterns of $CrSi_2$-r measured at different χ rotations and at $\phi = 0°$, First Brillouin zone of $CrSi_2$ and Calculated thermal dependence of the Seebeck coefficient of $CrSi_2$ using two different theoretical models.
This material is available free of charge via the Internet at http://pubs.acs.org

References

(1) Wu, H. J.; Zhao, L.-D.; Zheng, F. S.; Wu, D.; Pei, Y. L.; Tong, X.; Kanatzidis, M. G.; He, J. Q. Broad temperature plateau for thermoelectric figure of merit ZT>2 in phase-separated $PbTe_{0.7}S_{0.3}$. *Nat. Commun.* **2014**, *5*, 4515.

(2) Srinivasan, B.; Le Tonquesse, S.; Gellé, A.; Bourgès, C.; Monier, L.; Ohkubo, I.; Halet, J.-F.; Berthebaud, D.; Mori, T. Screening of Transition (Y, Zr, Hf, V, Nb, Mo, Ru) and Rare-earth (La, Pr) Elements as Potential Effective Dopants for Thermoelectric GeTe – an Experimental and Theoretical Appraisal. *J. Mater. Chem. A* **2020**, *8*, 19805–19821.

(3) Liu, W.; Wang, D.; Liu, Q.; Zhou, W.; Shao, Z.; Chen, Z. High-Performance GeTe-Based Thermoelectrics: from Materials to Devices. *Adv. Energy Mater.* **2020**, *10*, 2000367.

(4) Muchtar, A. R.; Srinivasan, B.; Tonquesse, S. L.; Singh, S.; Soelami, N.; Yuliarto, B.; Berthebaud, D.; Mori, T. Physical Insights on the Lattice Softening Driven Mid-Temperature Range Thermoelectrics of Ti/Zr-Inserted SnTe-An Outlook Beyond the Horizons of Conventional Phonon Scattering and Excavation of Heikes' Equation for Estimating Carrier Properties. *Adv. Energy Mater.* **2021**, *11*, 2101122.

(5) Rogl, G.; Grytsiv, A.; Rogl, P.; Peranio, N.; Bauer, E.; Zehetbauer, M.; Eibl, O. n-Type skutterudites $(R,Ba,Yb)_yCo_4Sb_{12}$ (R = Sr, La, Mm, DD, SrMm, SrDD) approaching ZT $\approx$ 2.0. *Acta Mater.* **2014**, *63*, 30 – 43.

(6) Zheng, Z.-H.; Shi, X.-L.; Ao, D.-W.; Liu, W.-D.; Chen, Y.-X.; Li, F.; Chen, S.; Tian, X.-Q.; Li, X.-R.; Duan, J.-Y.; Ma, H.-L.; Zhang, X.-H.; Liang, G.-X.; Fan, P.; Chen, Z.-G. Rational band engineering and structural manipulations inducing high thermoelectric performance in n-type $CoSb_3$ thin films. *Nano Energy* **2021**, *81*, 105683.

(7) Zhao, L.-D.; Lo, S.-H.; Zhang, Y.; Sun, H.; Tan, G.; Uher, C.; Wolverton, C.; Dravid, V. P.; Kanatzidis, M. G. Ultralow thermal conductivity and high thermoelectric figure of merit in SnSe crystals. *Nature* **2014**, *508*, 373–377.

(8) Chen, Y.-X.; Shi, X.-L.; Zheng, Z.-H.; Li, F.; Liu, W.-D.; Chen, W.-Y.; Li, X.-R.; Liang, G.-X.; Luo, J.-T.; Fan, P.; Chen, Z.-G. Two-dimensional WSe_2/SnSe p-n junctions secure ultrahigh thermoelectric performance in n-type Pb/I Co-doped polycrystalline SnSe. *Mater. Today Phys.* **2021**, *16*, 100306.

(9) LeBlanc, S.; Yee, S. K.; Scullin, M. L.; Dames, C.; Goodson, K. E. Material and manufacturing cost considerations for thermoelectrics. *Renew. Sust. Energ. Rev.* **2014**, *84*, 313–317.

(10) Skomedal, G.; Holmgren, L.; Middleton, H.; Eremin, I.; Isachenko, G.; Jaegle, M.; Tarantik, K.; Vlachos, N.; Manoli, M.; Kyratsi, T.; Berthebaud, D.; Truong, N. Y. D.; Gascoin, F. Design, assembly and characterization of silicide-based thermoelectric modules. *Energy Convers. Manag.* **2016**, *110*, 13–21.

(11) Graff, J. S.; Schuler, R.; Song, X.; Castillo-Hernandez, G.; Skomedal, G.; Enebakk, E.; Wright, D. N.; Stange, M.; de Boor, J.; Løvvik, O. M.; Schrade, M. Fabrication of a Silicide Thermoelectric Module Employing Fractional Factorial Design Principles. *J. Electron. Mater.* **2021**, *50*, 4041–4049.

(12) Le Tonquesse, S.; Matsushita, Y.; Jood, P.; Ohta, M.; Mori, T.; Berthebaud, D. Fabrication and Evaluation of Low-Cost $CrSi_2$ Thermoelectric Legs. *Crystals* **2021**, *11*, 1140.

(13) Aixala, L.; de Vaulx, C. Waste heat recovery by thermoelectricity on passenger car and heavy-duty truck diesel engine: the RENOTER project. *Diesel Powertrain Innovative Technologies for Future Emissions, France* **2012**, *1*, 1–8.

(14) Pichon, P.-Y. et al. Stability and thermoelectric performance of doped higher manganese silicide materials solidified by RGS (ribbon growth on substrate) synthesis. *J. Alloys Compd.* **2020**, *832*, 154602.

(15) Ihou Mouko, H.; Romanjek, K.; Mejri, M.; Oulfarsi, M.; El Oualid, S.; Malinconi, P.; Thimont, Y.; Malard, B.; Estournès, C.; David, N.; Dauscher, A. Manufacturing and performances of silicide-based thermoelectric modules. *Energ. Convers. Manag.* **2021**, *242*, 114304.

(16) Burkov, A. T. Silicide Thermoelectrics: Materials for Energy Harvesting. *Phys. Status Solidi* **2018**, *215*, 1800105.

(17) Fedorov, M. I.; Isachenko, G. N. Silicides: Materials for thermoelectric energy conversion. *Jpn. J. Appl. Phys.* **2015**, *54*, 07JA05.

(18) Liu, W.-D.; Chen, Z.-G.; Zou, J. Eco-Friendly Higher Manganese Silicide Thermoelectric Materials: Progress and Future Challenges. *Adv. Energy Mater.* **2018**, *8*, 1800056.

(19) Nozariasbmarz, A.; Agarwal, A.; Coutant, Z. A.; Hall, M. J.; Liu, J.; Liu, R.; Malhotra, A.; Norouzzadeh, P.; Öztürk, M. C.; Ramesh, V. P.; Sargolzaeiaval, Y.; Suarez, F.; Vashaee, D. Thermoelectric silicides: A review. *Jpn. J. Appl. Phys.* **2017**, *56*, 05DA04.

(20) Nagai, H.; Takamatsu, T.; Iijima, Y.; Hayashi, K.; Miyazaki, Y. Effects of Ge substitution on thermoelectric properties of $CrSi_2$. *Jpn. J. Appl. Phys.* **2016**, *55*, 111801.

(21) Nagai, H.; Takamatsu, T.; Iijima, Y.; Hayashi, K.; Miyazaki, Y. Effects of Nb substitution on thermoelectric properties of $CrSi_2$. *J. Alloys Compd.* **2016**, *687*, 37–41.

(22) Nagai, H.; Takamatsu, T.; Iijima, Y.; Hayashi, K.; Miyazaki, Y. Improved thermoelectric performance from $CrSi_2$ by Cu substitution into Si sites. *Jpn. J. Appl. Phys.* **2018**, *57*, 121801.

(23) Truong, D. Y. N.; Kleinke, H.; Gascoin, F. Preparation of pure Higher Manganese Silicides through wet ball milling and reactive sintering with enhanced thermoelectric properties. *Intermetallics* **2015**, *66*, 127–132.

(24) Khalil, M.; Moll, A.; Godfroy, M.; Letrouit-Lebranchu, A.; Villeroy, B.; Alleno, E.; Viennois, R.; Beaudhuin, M. Thermoelectric properties and stability of nanostructured chromium disilicide $CrSi_2$. *J. Appl. Phys.* **2019**, *126*, 135103.

(25) Mori, T.; Aizawa, T.; Vijayaraghavan, S. N.; Sato, N. Fabrication and Thermoelectric Properties of Chromium Silicide Thin Films. *Sens. Mater.* **2020**, *32*, 2433–2441.

(26) Li, Z.; Dong, J.-F.; Sun, F.-H.; Hirono, S.; Li, J.-F. Significant Enhancement of the Thermoelectric Performance of Higher Manganese Silicide by Incorporating MnTe Nanophase Derived from Te Nanowire. *Chem. Mater.* **2017**, *29*, 7378–7389.

(27) Norizan, M. N.; Miyazaki, Y.; Ohishi, Y.; Muta, H.; Kurosaki, K.; Yamanaka, S. The Nanometer-Sized Eutectic Structure of $Si/CrSi_2$ Thermoelectric Materials Fabricated by Rapid Solidification. *J. Electron. Mater.* **2018**, *47*, 2330–2336.

(28) Li, Z.; Dong, J.-F.; Sun, F.-H.; Asfandiyar,; Pan, Y.; Wang, S.-F.; Wang, Q.; Zhang, D.; Zhao, L.; Li, J.-F. MnS Incorporation into Higher Manganese Silicide Yields a Green Thermoelectric Composite with High Performance/Price Ratio. *Adv. Sci.* **2018**, *5*, 1800626.

(29) Perumal, S.; Gorsse, S.; Ail, U.; Prakasam, M.; Rajasekar, P.; Umarji, A. M. Enhanced thermoelectric figure of merit in nano-structured Si dispersed higher manganese silicide. *Mater. Sci. Semicond. Process.* **2019**, *104*, 104649.

(30) Kim, G.; Kim, H.-S.; Lee, H. S.; Kim, J.; Lee, K. H.; Roh, J. W.; Lee, W. Synchronized enhancement of thermoelectric properties of higher manganese silicide by introducing Fe and Co nanoparticles. *Nano Energy* **2020**, *72*, 104698.

(31) Yamamoto, A.; Ghodke, S.; Miyazaki, H.; Inukai, M.; Nishino, Y.; Matsunami, M.; Takeuchi, T. Thermoelectric properties of supersaturated Re solid solution of higher manganese silicides. *Jpn. J. Appl. Phys.* **2016**, *55*, 020301.

(32) Homma, T.; Kamata, T.; Saito, N.; Ghodke, S.; Takeuchi, T. Effects of Re substitution for Mn on microstructures and properties in Re-substituted higher manganese silicide thermoelectric material. *J. Alloys Comp.* **2019**, *776*, 8–15.

(33) Federov, M.; Zaitsev, V. In *Thermoelectrics Handbook*; Rowe, D., Ed.; CRC Press: Boca Raton, 2017.

(34) Solomkin, F. Y.; Zaitsev, V. K.; Novikov, S. V.; Samunin, Y. A.; Isachenko, G. N. Homogeneity domain and thermoelectric properties of $CrSi_2$. *Tech. Phys.* **2013**, *58*, 289–293.

(35) Kawasumi, I.; Sakata, M.; Nishida, I.; Masumoto, K. Crystal growth of manganese silicide, $MnSi_{\sim 1.73}$ and semiconducting properties of $Mn_{15}Si_{26}$. *J. Mater. Sci.* **1981**, *16*, 355–366.

(36) Sadia, Y.; Aminov, Z.; Mogilyansky, D.; Gelbstein, Y. Texture anisotropy of higher manganese silicide following arc-melting and hot-pressing. *Intermetallics* **2016**, *68*, 71–77.

(37) Vives, S. Microstructure control and transport properties of incommensurate manganese silicide based alloys for thermoelectricity. PhD thesis, Université de Bordeaux, France, 2015.

(38) Yamauchi, K.; Hagio, T.; Mitsuo, T.; Iwai, K.; Itoh, T. Thermoelectric properties of crystal aligned higher manganese silicide fabricated by solidification under magnetic field. *Jpn. J. Appl. Phys.* **2015**, *54*, 117102.

(39) Tan, C.; Tan, X.; Yu, B.; Liu, G.-Q.; Wang, H.; Luo, G.; Xu, J.; Wu, Q.; Liang, B.; Jiang, J. Synergistically Optimized Thermoelectric Performance in $Bi_{0.48}Sb_{1.52}Te_3$ by Hot Deformation and Cu Doping. *ACS Appl. Energy Mater.* **2019**, *2*, 6714–6719.

(40) Prasad, R.; Bhame, S. D. Review on texturization effects in thermoelectric oxides. *Mater. Renew. Sustain. Energy* **2020**, *9*, 3.

(41) Sui, J.; Li, J.; He, J.; Pei, Y.-L.; Berardan, D.; Wu, H.; Dragoe, N.; Cai, W.; Zhao, L.-D. Texturation boosts the thermoelectric performance of BiCuSeO oxyselenides. *Energy Environ. Sci.* **2013**, *6*, 2916–2920.

(42) Le Ferrand, H. Magnetic slip casting for dense and textured ceramics: A review of current achievements and issues. *J. Eur. Ceram. Soc.* **2021**, *41*, 24–37.

(43) Suzuki, T. S.; Miwa, Y.; Kawada, S.; Kimura, M.; Uchikoshi, T.; Sakka, Y. Two-dimensional orientationo in $Bi_4Ti_3O_{12}$ prepared using platelet particles and a magnetic field. *J. Am. Ceram. Soc.* **2013**, *96*, 1085–1089.

(44) Suzuki, T. S.; Suzuki, Y.; Uchikoshi, T.; Sakka, Y. Triaxial crystalline orientation of $MgTi_2O_5$ achieved using a strong magnetic field and geometric effect. *J. Am. Ceram. Soc.* **2016**, *99*, 1852–1854.

(45) Grasso, S.; Hu, C.; Vasylkiv, O.; Suzuki, T. S.; Guo, S.; Nishimura, T.; Sakka, Y. High-hardness B_4C textured by a strong magnetic field technique. *Scripta Mater.* **2011**, *64*, 256–259.

(46) Hu, C.; Sakka, Y.; Grasso, S.; Suzuki, T. S.; Tanaka, H. Tailoring Ti_3SiC_2 ceramic via a strong magnetic field alignment method followed by Spark Plasma Sintering. *J. Am. Ceram. Soc.* **2011**, *94*, 742–748.

(47) Suzuki, T. S.; Uchikoshi, T.; Sakka, Y. Effect of sintering conditions on microstructure

orientation in α-SiC prepared by slip casting in a strong magnetic field. *J. Eur. Ceram. Soc.* **2010**, *30*, 2813–2817.

(48) Zhu, X.; Suzuki, T. S.; Uchikoshi, T.; Nishimura, T.; Sakka, Y. Texture Development in Si_3N_4 Ceramics by Magnetic Field Alignment during Slip Casting. *J. Ceram. Soc. Japan* **2006**, *114*, 979–987.

(49) Suzuki, T. S.; Uchikoshi, T.; Sakka, Y. Effect of sintering additive on crystallographic orientation in AlN prepared by slip casting in a strong magnetic field. *J. Eur. Ceram. Soc.* **2009**, *29*, 2627–2633.

(50) Wu, W.-W.; Sakka, Y.; Estili, M.; Suzuki, T. S.; Nishimura, T.; Zhang, G.-J. Microstructure and high-temperature strength of textured and non-textured ZrB_2 ceramics. *Sci. Technol. Adv. Mater.* **2014**, *15*, 014202.

(51) Kaga, H.; Kinemuchi, Y.; Watari, K.; Tanaka, S.; Makiya, A.; Kato, Z.; Uematsu, K. Fabrication of c -axis oriented higher manganese silicide by a high-magnetic-field and its thermoelectric properties. *J. Mater. Res.* **2007**, *22*, 2917–2923.

(52) Wu, W.-W.; Sakka, Y.; Suzuki, T. S.; Zhang, G.-J. Microstructure and anisotropic properties of textured ZrB_2 and ZrB_2-$MoSi_2$ ceramics prepared by strong magnetic field alignment. *Int. J. Appl. Ceram. Tec.* **2014**, *11*, 218–227.

(53) Le Tonquesse, S.; Dorcet, V.; Joanny, L.; Demange, V.; Prestipino, C.; Guo, Q.; Berthebaud, D.; Mori, T.; Pasturel, M. Mesostructure - thermoelectric properties relationships in $V_xMn_{1-x}Si_{1.74}$ (x = 0, 0.04) Higher Manganese Silicides prepared by magnesiothermy. *J. Alloys Compd.* **2020**, *816*, 152577.

(54) Le Tonquesse, S.; Joanny, L.; Guo, Q.; Elkaim, E.; Demange, V.; Berthebaud, D.; Mori, T.; Pasturel, M.; Prestipino, C. Influence of Stoichiometry and Aging at Operating Temperature on Thermoelectric Higher Manganese Silicides. *Chem. Mater.* **2020**, *32*, 10601–10609.

(55) Le Tonquesse, S.; Verastegui, Z.; Huynh, H.; Dorcet, V.; Guo, Q.; Demange, V.; Prestipino, C.; Berthebaud, D.; Mori, T.; Pasturel, M. Magnesioreduction Synthesis of Co-Doped β-$FeSi_2$: Mechanism, Microstructure, and Improved Thermoelectric Properties. *ACS Appl. Energy Mater.* **2019**, *12*, 8525–8534.

(56) Lutterotti, L.; Matthies, S.; Wenk, H.-R. MAUD (Material Analysis Using Diffraction): a user friendly Java program for Rietveld Texture Analysis and more. *Proceeding of the Twelfth International Conference on Textures of Materials (ICOTOM-12)* **1999**, *1*, 1599.

(57) Giannozzi, P. et al. QUANTUM ESPRESSO: a modular and open-source software project for quantum simulations of materials. *J. Phys. Condens. Matter* **2009**, *21*, 395502.

(58) Giannozzi, P. et al. Advanced capabilities for materials modelling with Quantum ESPRESSO. *J. Phys. Condens. Matter* **2017**, *29*, 465901.

(59) Perdew, J. P.; Burke, K.; Ernzerhof, M. Generalized Gradient Approximation Made Simple. *Phys. Rev. Lett.* **1996**, *77*, 3865–3868.

(60) Kresse, G.; Joubert, D. From ultrasoft pseudopotentials to the projector augmented-wave method. *Phys. Rev. B* **1999**, *59*, 1758–1775.

(61) Monkhorst, H. J.; Pack, J. D. Special points for Brillouin-zone integrations. *Phys. Rev. B* **1976**, *13*, 5188–5192.

(62) Pack, J. D.; Monkhorst, H. J. Special points for Brillouin-zone integrations–a reply. *Phys. Rev. B* **1977**, *16*, 1748–1749.

(63) Mostofi, A. A.; Yates, J. R.; Lee, Y.-S.; Souza, I.; Vanderbilt, D.; Marzari, N. wannier90: A tool for obtaining maximally-localised Wannier functions. *Comput. Phys. Commun.* **2008**, *178*, 685–699.

(64) Pizzi, G. et al. Wannier90 as a community code: new features and applications. *J. Phys. Condens. Matter* **2020**, *32*, 165902.

(65) Scheidemantel, T. J.; Ambrosch-Draxl, C.; Thonhauser, T.; Badding, J. V.; Sofo, J. O. Transport coefficients from first-principles calculations. *Phys. Rev. B* **2003**, *68*, 125210.

(66) Dronskowski, R.; Bloechl, P. E. Crystal orbital Hamilton populations (COHP): energy-resolved visualization of chemical bonding in solids based on density-functional calculations. *J. Phys. Chem.* **1993**, *97*, 8617–8624.

(67) Deringer, V. L.; Tchougréeff, A. L.; Dronskowski, R. Crystal Orbital Hamilton Population (COHP) Analysis As Projected from Plane-Wave Basis Sets. *J. Phys. Chem. A* **2011**, *115*, 5461–5466.

(68) Maintz, S.; Deringer, V. L.; Tchougréeff, A. L.; Dronskowski, R. Analytic projection from plane-wave and PAW wavefunctions and application to chemical-bonding analysis in solids. *J. Comput. Chem.* **2013**, *34*, 2557–2567.

(69) Maintz, S.; Deringer, V. L.; L. Tchougréeff, A.; Dronskowski, R. LOSTER A tool to extract chemical bonding from plane-wave based DFT. *J. Comput. Chem.* **2016**, *37*, 1030–1035.

(70) Kittel, C.; McEuen, P. *Introduction to Solid State Physics*; 9th ed. Wiley: New Jersey, 2018.

(71) Ohsugi, I. J.; Kojima, T.; Nishida, I. A. Temperature dependence of the magnetic susceptibility of a $CrSi_2$ single crystal. *Phys. Rev. B* **1990**, *42*, 10761–10764.

(72) Nishida, I. The crystal growth and thermoelectric properties of chromium disilicide. *J. Mater. Sci.* **1972**, *7*, 1119–1124.

(73) Guilmeau, E.; Chateigner, D.; Suzuki, T. S.; Sakka, Y.; Henrist, C.; Ouladdiaf, B. Rietveld texture analysis of alumina ceramics by neutron diffraction. *Chem. Mater.* **2005**, *17*, 102–106.

(74) Yamada, H.; Suzuki, T. S.; Uchikoshi, T.; Hozumi, M.; Kohama, K.; Sakka, Y. Fabrication and analysis of the oriented $LiCoO_2$ by slip-casting in a strong magnetic field. *J. Am. Ceram. Soc.* **2012**, *95*, 1–6.

(75) Yansheng, L.; Fu, W.; Jiazheng, X.; Zhide, L. Estimation of the true orientation distribution function determination of the maximum-entropy method by the Taylor model. *J. Apply. Cryst.* **1993**, *26*, 268–271.

(76) Chateigner, D. *Combined Analysis*; ISTE Ltd, Wiley: London, Hoboken, 2010.

(77) Dasgupta, T.; Etourneau, J.; Chevalier, B.; Matar, S. F.; Umarji, A. M. Structural, thermal, and electrical properties of $CrSi_2$. *J. Appl. Phys.* **2008**, *103*, 113516.

(78) Voronov, B. K.; Dudkin, L. D.; Trusova, N. N. In *Chemical Bonds in Solids: Volume 4: Semiconductor Crystals, Glasses, and Liquids*; Sirota, A. N. N., Ed.; Springer US: New York, NY, 1972; pp 21–26.

(79) Nakasawa, H.; Takamatsu, T.; Iijima, Y.; Hayashi, K.; Miyazaki, Y. Thermoelectric Properties of Mo and Ge co-substituted $CrSi_2$. *Trans. Mater. Res. Soc. Japan* **2018**, *43*, 85–91.

(80) Nakasawa, H.; Hayashi, K.; Takamatsu, T.; Miyazaki, Y. Lattice dynamics and lattice thermal conductivity of $CrSi_2$ calculated from first principles and the phonon Boltzmann transport equation. *J. Appl. Phys.* **2019**, *126*, 025105.

(81) Lasjaunias, J. C.; Gottlieb, U.; Laborde, O.; Thomas, O.; Madar, R. Transport and low temperature specific heat measurement of $CrSi_2$ single crystal. *MRS Proc.* **1995**, *402*, 343–348.

(82) Casimir, H.; Gerritsen, A. The electric resistance of single crystals of bismuth in a magnetic field. *Physica* **1941**, *8*, 1107–1112.

(83) Akgoz, Y. C.; Saunders, G. A. Space-time symmetry restrictions on the form of transport tensors. I. Galvanomagnetic effects. *J. Phys. C* **1975**, *8*, 1387–1396.

(84) Alleno, E. et al. A round robin test of the uncertainty on the measurement of the thermoelectric dimensionless figure of merit of $Co_{0.97}Ni_{0.03}Sb_3$. *Rev. Sci. Instrum.* **2015**, *86*, 011301.

(85) Mattheiss, L. F. Electronic structure of $CrSi_2$ and related refractory disilicides. *Phys. Rev. B* **1991**, *43*, 12549–12555.

(86) Bost, M. C.; Mahan, J. E. An investigation of the optical constants and band gap of chromium disilicide. *J. Appl. Phys.* **1988**, *63*, 839–844.

(87) Bellani, V.; Guizzetti, G.; Marabelli, F.; Piaggi, A.; Borghesi, A.; Nava, F.; Antonov, V. N.; Antonov, V. N.; Jepsen, O.; Andersen, O. K.; Nemoshkalenko, V. V. Theory and experiment on the optical properties of $CrSi_2$. *Phys. Rev. B* **1992**, *46*, 9380–9389.

(88) Dennis, J. H. Anisotropy of the Seebeck Coefficient of Bismuth Telluride. *Adv. Energy Convers.* **1961**, *1*, 99–105.

(89) Bies, W. E.; Radtke, R. J.; Ehrenreich, H.; Runge, E. Thermoelectric properties of anisotropic semiconductors. *Phys. Rev. B* **2002**, *65*, 085208.

(90) Chasapis, T. C.; Lee, Y.; Hatzikraniotis, E.; Paraskevopoulos, K. M.; Chi, H.; Uher, C.; Kanatzidis, M. G. Understanding the role and interplay of heavy-hole and light-hole valence bands in the thermoelectric properties of PbSe. *Phys. Rev. B* **2015**, *91*, 085207.

(91) Sun, H.; Lu, X.; Chi, H.; Morelli, D. T.; Uher, C. Highly efficient $(In_2Te_3)_x(GeTe)_{3-3x}$ thermoelectric materials: a substitute for TAGS. *Phys. Chem. Chem. Phys.* **2014**, *16*, 15570–15575.

Graphical TOC Entry